

Deep Interactive Denoiser (DID) for X-Ray Computed Tomography

Ti Bai, Biling Wang, Dan Nguyen, Bao Wang, Bin Dong, Wenxiang Cong, Mannudeep K. Kalra, and Steve Jiang

Abstract—Low dose computed tomography (LDCT) is desirable for both diagnostic imaging and image guided interventions. Denoisers are openly used to improve the quality of LDCT. Deep learning (DL)-based denoisers have shown state-of-the-art performance and are becoming one of the mainstream methods. However, there exists two challenges regarding the DL-based denoisers: 1) a trained model typically does not generate different image candidates with different noise-resolution tradeoffs which sometimes are needed for different clinical tasks; 2) the model generalizability might be an issue when the noise level in the testing images is different from that in the training dataset. To address these two challenges, in this work, we introduce a lightweight optimization process at the testing phase on top of any existing DL-based denoisers to generate multiple image candidates with different noise-resolution tradeoffs suitable for different clinical tasks in real-time. Consequently, our method allows the users to interact with the denoiser to efficiently review various image candidates and quickly pick up the desired one, and thereby was termed as deep interactive denoiser (DID). Experimental results demonstrated that DID can deliver multiple image candidates with different noise-resolution tradeoffs, and shows great generalizability regarding various network architectures, as well as training and testing datasets with various noise levels.

Index Terms—Deep Learning, Computed Tomography, Image Denoising

I. INTRODUCTION

MEDICAL imaging techniques have been playing vital roles in healthcare for disease diagnosis and clinical procedure guidance. However, their clinical value can be heavily decreased if the produced medical images cannot faithfully reflect the clinical realities due to image quality degradations. To be specific, regarding X-ray computed tomography (CT), quantum noise is one of the dominant degradation factors due to the low-dose irradiation demand. A strong quantum noise might overwhelm potential low-contrast lesions, making the disease diagnosis or procedure guidance very challenging. Therefore, a denoiser is usually required to enhance the image quality by suppressing the noise effectively while preserving the image resolution as much as possible.

Ti Bai, Dan Nguyen, Biling Wang and Steve Jiang (corresponding author) were with Medical Artificial Intelligence and Automation (MAIA) Laboratory, Department of Radiation Oncology, University of Texas Southwestern Medical Centre, Dallas, Texas 75239, USA (e-mail: Ti.Bai@UTSouthwestern.edu, Dan.Nguyen@UTSouthwestern.edu, Biling.Wang@UTSouthwestern.edu, Steve.Jiang@UTSouthwestern.edu).

Bao Wang was with Department of Mathematics and Scientific Computing and Imaging Institute, University of Utah, Salt Lake City, UT, USA (e-mail: bwang@math.utah.edu)

Bin Dong was with Beijing International Center for Mathematical Research, Peking University, Beijing, China (e-mail: dongbin@math.pku.edu.cn)

Wenxiang Cong was with Department of Biomedical Engineering, Rensselaer Polytechnic Institute, Troy, NY, 12180, USA. (e-mail: wxcong@gmail.com)

Mannudeep K. Kalra was with Department of Radiology, Massachusetts General Hospital and Harvard Medical School, Boston, MA, USA (e-mail: mkalra@mgh.harvard.edu)

Denoising is a long-standing problem in the X-ray CT imaging field, and thus accordingly has resulted in abundant research [1]–[22]. In recent years, deep learning (DL) techniques witnessed unprecedented success in many fields [23]–[35], and were also widely employed for medical image denoising [1], [4], [12], [13], [20], [22]. For instance, Chen *et al.* built a residual encoder-decoder convolutional neural network (CNN) to enhance the low-dose CT (LDCT) image quality [10]. Shan *et al.* demonstrated a 3D CNN for volumetric CT image denoising which can be pretrained from a 2D version [22]. Yang *et al.* used a generative adversarial network (GAN) to denoise the CT images [13]. Li *et al.* proposed a multi-stage network to gradually improve the enhanced CT images [12]. Since the deep learning methods can automatically learn powerful features directly from the existed database, which usually exhibit stronger expressiveness compared to the models manually designed by human experts, they have superior denoising performance than the conventional methods, and accordingly become a mainstream method.

Despite the great progress, there still exist some problems needed to be solved regarding the DL-based denoisers before they can be widely deployed in real clinical practice. First, a major problem is regarding model generalizability. Theoretically speaking, to maximize the denoising performance, DL-based denoisers are best used to denoise images that have the noise levels that existed in the training dataset. In other words, a denoiser can only reach its maximum performance when the training and testing domains exactly match. For example, to have the optimal denoising performance for the CT images acquired at a certain low-dose level, the desired network should be trained by feeding the LDCT images with the same low-dose level into the network to predict the full-dose level CT images. In this regard, one can train multiple models to aim at different noise levels by using different training datasets. However, one can hardly consider all the noise levels in model training because, in clinical practice, there are too many factors contributing to the noise level, such as different anatomical sites, equipment vendors, and imaging protocols.

Second, it is well-accepted that medical image quality is highly task-specific, and sometimes observer-specific, because different tasks require different noise-resolution tradeoffs and different observers with different clinical backgrounds have their own tradeoff preferences even for the same clinical tasks. Therefore, a good practical denoiser should be able to produce multiple images with different noise-resolution tradeoffs such that the user can pick the desired one. This can be relatively easily achieved with a conventional regularized iterative algorithm [2], [6], [7], [9], [15]–[19], [21], [36], [37], where regularization parameters can be adjusted to generate a noise-resolution tradeoff (NRT) curve consisting of denoised

images with various noise-resolution tradeoffs to meet various clinical demands. However, due to their black-box nature, most of the DL-based denoisers do not have this clinically significant feature.

To our best knowledge, little effort has been made to solve the above two clinically important problems regarding the DL-based CT denoisers. The most relevant work came from Shan *et al.*, who proposed a modularized adaptive processing neural network (MAP-NN) [20]. In that work, the authors proposed a unique training framework which can modulate the denoising direction by designing a module-clone-based network architecture. Once the MAP-NN is well-trained, each single module can suppress the noise at a small step. Thereby, the trained denoiser can produce multiple images to meet the user's preference.

Since many groups have developed DL-based CT denoisers that can deliver state-of-the-art results, it will be of great value if one can solve the above mentioned two problems by adding a light plug-in to their developed denoisers. In this study, our purpose is to develop such a light plug-in to empower any existing DL-based CT denoisers with the capabilities that: 1) can allow users to interactively and continuously adjust the noise-resolution tradeoff; 2) can adapt to the new testing images which have different noise levels from the training images. The proposed method, termed as deep interactive denoiser (DID), is part of our efforts of developing human-centered artificial intelligence (AI) in medicine. We believe in many challenging clinical scenarios, AI should assist human experts to make clinical decisions or perform clinical procedures better and faster, not try to replace human experts by fully automating everything. In the proposed LDCT denoising applications, DID will assist users to interactively tune the images to achieve the noise-resolution tradeoff desired for the specific task and particular user. It should be noted that DID is directly used in the model testing phase, does not require a training stage, and hence can be readily combined with any existing DL-based denoisers.

II. METHODS AND MATERIALS

A. Methods

Let us first mathematically formulate the X-ray CT denoising problem. Basically, given a noisy image $x \in \mathbb{R}^N$, the denoising task is to restore the underlying clean counterpart $y \in \mathbb{R}^N$, where the images are vectorized representations and N denotes the number of the pixels. If the noise $\epsilon \in \mathbb{R}^N$ is assumed to be additive, we have:

$$x = y + \epsilon. \quad (1)$$

The above problem can be effectively solved in a learning-and-prediction fashion. More specifically, in the context of DL-based denoising methods, a CNN ϕ_w parameterized by w can be learned from a training dataset $\{(x_m, y_m) | m \in (0, 1, \dots, M-1)\}$ with a size of M , where m indexes the noisy-clean image pairs, by minimizing the following cost functions:

$$w_0 = \arg \min_w \sum_{m=0}^{M-1} \|\phi_w(x_m) - y_m\|_2^2. \quad (2)$$

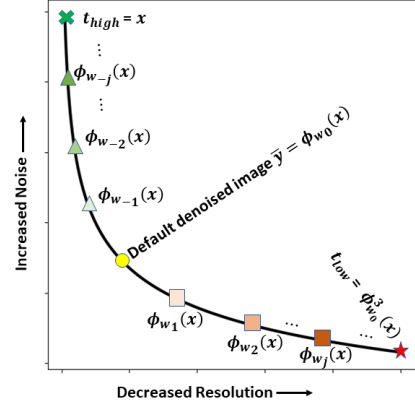


Fig. 1. Illustration of the main idea of the proposed DID algorithm. We assume all denoised images with different noise-resolution tradeoffs fall on a noise-resolution tradeoff curve. The default denoised image $\bar{y} = \phi_{w_0}(x)$ (yellow circle) is generated by a pre-trained DL-based denoiser. Bound point t_{high} corresponds to an image with high resolution and high noise (green cross), and bound point t_{low} corresponds to an image with low resolution and low noise (red star). Two bound points are determined such that they bracket most, if not all, images with clinically meaningful noise-resolution tradeoffs. The images between t_{high} and \bar{y} (triangles) and the images between \bar{y} and t_{low} (squares) are all generated with the proposed DID algorithm.

Once the network training (learning) process is finished, a denoised image \bar{y} can be predicted by feeding a noisy image x into the network:

$$\bar{y} = \phi_{w_0}(x). \quad (3)$$

From (3), regarding the conventional model deployment, one can find that the learned CNN ϕ is a one-to-one mapping if the learned network parameters w_0 is fixed (which is also a common and default setting in practice) during the model testing phase.

Regarding this study, one of the purposes is to equip any existing DL-based denoisers with the feature that can dynamically produce denoised image with a desired noise-resolution tradeoff among all the achievable tradeoffs. To achieve this purpose, we propose a method to generate multiple denoised images with different noise-resolution tradeoffs based on a denoised image \bar{y} produced by a pre-trained DL-based denoiser ϕ_{w_0} for a given LDCT image x .

Fig. 1 illustrates the main idea of the proposed DID algorithm. We assume all denoised images with different noise-resolution tradeoffs can construct a NRT curve, and most, if not all, images denoised from a LDCT image x with clinically meaningful noise-resolution tradeoffs can be bracketed with two bound points t_{high} and t_{low} , where t_{high} corresponds to a denoised image with high resolution and high noise and t_{low} corresponds to a denoised image with low resolution and low noise. The default denoised image $\bar{y} = \phi_{w_0}(x)$ generated by a pre-trained DL-based denoiser ϕ_{w_0} falls between t_{high} and t_{low} . The goal of the proposed DID algorithm is to populate this NRT curve between t_{high} and t_{low} using the three known points: \bar{y} , t_{high} , and t_{low} .

In this work, we choose the original noisy LDCT image x as t_{high} , representing the highest resolution and highest noise since it is very unlikely someone wants to add more noise to the original noisy image. To generate t_{low} , we purposely overly denoise x by recursively applying pre-trained DL-based denoiser ϕ_{w_0} for K times: $t_{\text{low}} = \phi_{w_0}^K(x) =$

$\phi_{w_0}(\dots(\phi_{w_0}(x)))$, where K is determined empirically such that it is the smallest number while can still ensure t_{low} has the lowest resolution and lowest noise than any images with clinically meaningful noise-resolution tradeoffs. In this work, we found $K = 3$.

To populate the NRT curve between t_{high} and t_{low} , we will fine-tune the pre-trained denoiser ϕ_{w_0} by solving the following problems:

$$w = \arg \min_w \|\phi_w(x) - t_{\text{low}}\|_2^2, \quad (4)$$

$$w = \arg \min_w \|\phi_w(x) - t_{\text{high}}\|_2^2. \quad (5)$$

Problems (4) and (5) can be efficiently iteratively solved with the gradient descent algorithm. During the optimization process, a series of network parameters $w_0, w_{\pm 1}, \dots, w_{\pm J}$ from different iterations can be generated, where w_0 is the starting point with respect to the pre-trained denoising network ϕ_{w_0} . Here we use w_1, \dots, w_J to denote those images generated by solving problem (4), which have lower resolution and lower noise than the default denoised image $\bar{y} = \phi_{w_0}(x)$. We use w_{-1}, \dots, w_{-J} to denote those images generated by solving problem (5), which have higher resolution and higher noise than the default denoised image $\bar{y} = \phi_{w_0}(x)$.

It is well-accepted that deep neural network is very easy to fit a wide variety of functions considering its large model capacity. Since minimizing cost function (4) in the testing phase equals to train a network with a training dataset consisting of only one sample (x, t_{low}) , this “one sample” training dataset is very easy to be overfitted. As a result, it is expected that $\phi_{w_J}(x) = t_{\text{low}}$ when the optimization process is converged. During this optimization process, we observed that the network’s output with updated model parameters w_1, \dots, w_J will gradually transit from the initial image $\phi_{w_0}(x)$ to the final target image $t_{\text{low}} = \phi_{w_J}(x)$. Basically, t_{low} guides the network parameters to be updated in a specified direction towards lower noise and lower resolution, such that the associated network output $\phi_{w_1}(x), \dots, \phi_{w_J}(x)$ will populate the NRT curve between \bar{y} and t_{low} and exhibit noise-resolution tradeoffs with gradually lower resolution and lower noise. The reasoning for populating the NRT curve between t_{high} and \bar{y} by minimizing cost function (5) is similar. Fig. 2 provides a simple illustration about this process.

In this work, we would also provide a heuristic argument to further show that the intermediate results $\phi_{w_{\pm 1}}(x), \phi_{w_{\pm 2}}(x) \dots \phi_{w_{\pm J}}(x)$ exhibit monotonic noise and resolution changes.

Let $L(w) := \|\phi_w(x) - t\|_2^2$, for any given pair (x, t) . Consider gradient flow

$$w_{j+1} = w_j - \eta \nabla L(w),$$

then by definition, we have that $L(w_j)$ monotonically decreases when the learning rate η small enough. When ϕ_w is over-parameterized, then by the theory of neural tangent kernel (NTK) [38], $L(w_j) \rightarrow 0$ exponentially as $j \rightarrow \infty$.

It was recently discovered that, in the NTK regime [39], the training dynamics minimizing $L(w)$ with gradient flow can be written as

$$\phi^{j+1} = \phi^j - \eta \Theta_x(\phi^j - t),$$

where we define $\phi^j = \phi_{w_j}(x)$ for clarity. This dynamics is identical to the procedure known as twicing [40] except that the choice of kernel Θ_x is different.

Suppose that x is a noisy image and t is a low resolution and low noise image (e.g. $t_{\text{low}} = \phi_{w_0}^3(x)$). Then, the algorithm starts with $\phi^0 = \phi_{w_0}(x)$ and $\phi^0 - t = \phi_{w_0}(x) - \phi_{w_0}^3(x) = \delta_1$ represents the noise (as well as some sharp features) that is still present in $\phi_{w_0}(x)$ which is gradually removed during the iteration. Similarly, suppose that t is a high resolution and high noise image (e.g. $t_{\text{high}} = x$ itself). Then, the algorithm starts with $\phi^0 = \phi_{w_0}(x)$ and $\phi^0 - t = \phi_{w_0}(x) - x = -\delta_2$ represents the sharp features (as well as noise) that is removed from $\phi_{w_0}(x)$ which is gradually injected back during the iteration.

As such, our DID algorithm now can use the bound images to guide the model parameters being modified from the pre-trained parameters w_0 towards two different directions with respect to different noise-resolution tradeoffs. It is expected that 1) the images generated towards the bound point t_{low} have lower noise and lower resolution that are preferred for tasks like low-contrast lesion detection, and 2) the images generated towards the bound point t_{high} have higher resolution and higher noise that are preferred for tasks like high-contrast structure inspection. It should be noted that the step size regarding the image generation is determined by the learning rate. Therefore, in theory, one can continuously control the noise-resolution tradeoff by choosing a very small learning rate.

III. MATERIALS

A. Datasets

1) *Training and validation datasets*: We used the public accessed X-ray Low-dose CT challenge dataset [41](<https://www.aapm.org/GrandChallenge/LowDoseCT>) to train the DL-based denoiser. More specifically, in the officially released training dataset, there are ten patients who were scanned with Siemens CT scanners. To simulate the LDCT image, Poisson noise was first inserted into the acquired helical projection data to reach a noise level that corresponds to 25% of the normal dose. Then, both the original normal-dose projection data and the simulated low-dose projection data were reconstructed into CT images, termed as normal-dose CT (NDCT) and LDCT, respectively. Each patient case contains around 600 2D slices. We further split the above ten patient cases into eight for training and two for validation. Finally, we have 4800 2D slices in the training dataset and 1136 2D slices in the validation dataset. The image size is of 512×512 .

2) *Testing datasets*: To further evaluate the proposed method with external datasets, we employed two different realistic datasets.

The first dataset was collected based on a cadaver study by using a GE CT scanner in Massachusetts General Hospital. In this study, a cadaver was scanned with four different exposure levels, such that the resulted CT images correspond to four different noise indexes (NIs), i.e., 10, 20, 30 and 40. All the CT images in this dataset were reconstructed with commercial software under default parameters settings.

The second dataset were based a realistic patient case suffering from the prostate cancer and receiving image guided

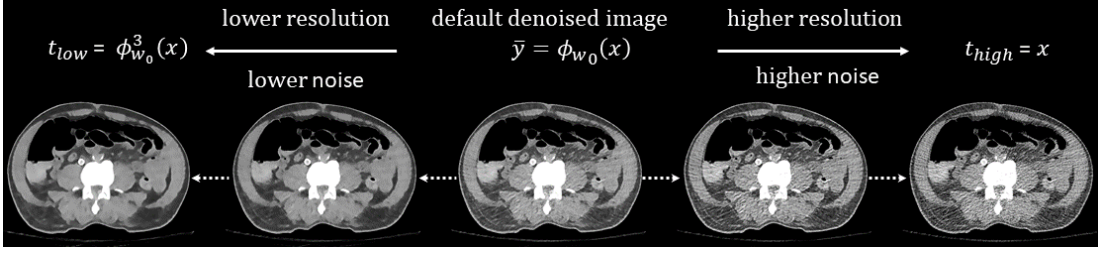


Fig. 2. Gradually transiting noise-resolution tradeoffs among the generated images from the proposed DID algorithm. The middle image is the default denoised image $\bar{y} = \phi_{w_0}(x)$. From middle to right, images with higher resolution are generated by solving problem (5). From middle to left, images with lower noise are generated by solving problem (4). Display window: [-160, 240] HU.

radiation therapy. It should be noted that this dataset was collected with a cone-beam CT (CBCT) imager integrated with a TrueBeam medical linear accelerator (Varian Medical System, Palo Alto, CA). In details, this dataset contains six CBCT scans collected in three consecutive treatment fractions. At each fraction, a low-dose CBCT scan was taken followed by a normal-dose CBCT scan. All the three normal-dose CBCT scans have an exposure setting of $80\text{mA} \times 13\text{mA}$, while the three different low-dose CBCT scans have exposure settings of $40\text{mA} \times 13\text{mA}$, $20\text{mA} \times 13\text{mA}$, and $10\text{mA} \times 13\text{mA}$. All the six projection datasets were FDK-reconstructed into CBCT images of size $512 \times 512 \times 256$ with a voxel size of $1.0 \times 1.0 \times 1.0 \text{ mm}^3$. A representative image was extracted for algorithm validation.

B. Experimental Design

1) *Denoiser in the training phase:* Without loss of generality, in this work, we used the well-known U-Net [42] to train the denoiser for algorithm demonstration purpose. Since the images in the training dataset has a size of 512×512 , the downsampling depth was set as 9 such that the bottleneck layer has a feature dimension of 1×1 . The feature doubling strategy was adopted in the upsampling stages. The initial feature channel was set as 32. Regarding the network modules, we used the instance normalization [43] technique as the normalization layer, and the rectified linear unit (ReLU) as the nonlinear activation layer. The convolutional operator has a kernel size of 3×3 . We use stride two convolution operator to conduct the downsampling operation.

The Adam [44] optimizer was employed to minimize the cost function defined in problem (2) by 1×10^5 iterations. The initial learning rate was set as 1×10^{-4} , and was reduced by 10 times at 5×10^4 and 7.5×10^4 iterations, such that the corresponding learning rates were 1×10^{-5} and 1×10^{-6} , respectively. The two hyper-parameters associated with the Adam optimizer were set as $\beta_1 = 0.9$ and $\beta_2 = 0.999$, respectively. The batch size was 1.

For clarity, herein after, without explicitly pointing out, the denoiser is referred to as the above U-Net denoiser.

2) *Interactive denoising in the testing phase:* As stated previously, given above pre-trained denoiser, by optimizing cost functions (4) and (5) with different guidance images in the testing phase, we can produce multiple images that exhibit different noise-resolution tradeoffs.

For all the experiments in the testing phase, the stochastic gradient descent (SGD) with 0.9 momentum was used. The learning rate was fixed as 1×10^{-2} . The optimization pro-

cess was terminated when the relative change between two consecutive output is less than 1%.

3) *Experiments:* We first conducted experiments based on the validation dataset which holds the same distribution as the training dataset. In details, to show the task-specific denoising, two 2D CT images were selected from the validation dataset, one of which contains many high-resolution structures while the other contains a low-contrast lesion. The associated default denoised images were produced by feeding these two noisy images into the pretrained denoiser. Both the two bound images t_{high} and t_{low} were generated. To show the gradually transiting property in terms of the noise-resolution tradeoff during the optimization processes regarding problems (4) and (5), we selected one image candidate representing the high-resolution direction and one candidate representing the low-noise direction. For comparison, we also show the default denoised image, the original input LDCT as well as the reference NDCT.

The root mean squared error (RMSE) was calculated against the associated NDCT for all the images. Moreover, for the low-contrast lesion detection task, we calculated the contrast-noise-ratio (CNR) of the lesion region of interest (ROI) for quantitative comparison. The CNR is calculated as $\text{CNR} = \frac{2|S - S_b|}{\sigma + \sigma_b}$, where S and S_b represent the mean intensities of the ROI and the background, σ and σ_b are the associated standard deviations.

We then demonstrated the performance of the proposed method on a realistic dataset based on the cadaver study. For this site, we have four CT slices associated with four different NIs, i.e., 10, 20, 30 and 40. Note that these four slices are not perfectly pixelwise matched since they were scanned at different time points. The proposed method was applied on all the four slices. We showed two representative image candidates corresponding to the high-resolution and the low-noise directions, as well as the default denoised image and the original input image. Same experiments were also carried out on the above-mentioned CBCT datasets who have three different exposure settings.

For each of the experiments, we manually selected a flat ROI to calculate the standard deviation (STD).

C. Ablation studies

1) *Different CNN architectures:* In this paper, the default denoiser is based on the widely used U-Net architecture. To verify the generalizability of our DID algorithm regarding network architecture, we further used a simpler while more

general architecture to train the denoiser. More specifically, this architecture contains eight consecutive convolutional layers without any downsampling or upsampling operators. Each layer is consisting of three operators: convolution operator with a kernel size of 3×3 , instance normalization operator and ReLU operator. As such, the input image size is the same as the output image size. We term this network as plain network.

All the other training details were the same as the U-Net-based denoiser. Similar evaluation experiments as above were conducted. In details, without loss of generality, the image associated with high-resolution structures from the validation dataset and the image associated with a NI of 30 from the cadaver study were used for algorithm verification. All the other experimental settings in the testing phase are the same as above.

2) Different training datasets with different noise levels:

Finally, to test the generalizability of the proposed DID algorithm regarding different training datasets with different noise levels, we trained four different denoisers with four different datasets. The difference among these training datasets were the low-dose levels. In details, in the original training datasets, each training image pair is consisting of a simulated quarter-dose-level LDCT and the associated NDCT. As such, we can get the associated noise component by subtracting the NDCT from the LDCT. Consequently, we can simulate the half-dose-level, $\frac{1}{8}$ -dose-level and $\frac{1}{16}$ -dose-level LDCTs by adding back half, twice, four-times of the noise into the NDCT, respectively. We then trained four different denoisers with these four (the above three plus the original dataset where the LDCTs have a quarter-dose-level) different datasets corresponding to four different noise levels. The architecture as well as the training details were the same as the default U-Net denoiser. We use the image associated with high-resolution structures from the validation dataset as the test image, which has a default 25% dose level compared to the NDCT.

IV. RESULTS

We illustrate in Fig. 3 an image from the validation dataset to show the different low-contrast lesion detectabilities regarding different denoised image candidates that have different noise-resolution tradeoffs. Since the detectability of the low-contrast structure is generally more sensitive to the noise strength, we show two different image candidates (a) and (b) along the low-noise processing direction. We can find that the detectability of the low-contrast lesion marked by the red dot box is higher and higher as more and more noise are suppressed, as suggested by the image candidates going from (d) to (a). This phenomenon can be verified from the associated zoomed-in view shown in Row 2 of Fig. 3, where this lesion is hardly perceived from the noisy LDCT. It should be noted that the default denoised image (c) is still over-noisy for this low-contrast detection clinical task. The low-noise image candidate (b) is the most similar to the NDCT image (f) in terms of the lesion's appearance, while the low-noise image candidate (a) shows the highest detectability, which can be more clearly observed from the zoomed-in view. For quantitative evaluation regarding the detectability of this low-contrast lesion, we calculate the CNR, where the foreground

and background contents are specified by the purple dot and the blue solid boxes, as indicated in the zoomed-in view in Fig. 3. As expected, as more and more noise are suppressed, the resultant CNRs are improved to be higher and higher, suggesting better and better detectability.

It is surprising that the CNR associated with NDCT image is 0.857, which is comparable with that of the default denoised image, despite that the visual quality of the default denoised image is much worse than that of NDCT image and also the low-noise image candidates. One possible reason might be that their noise strengths might be comparable while their noise textures are distinctly different. We further quantitatively check the STDs based on a flat region as marked by the green solid box in Fig. 3(f), Row 1. The resultant values are listed below each corresponding image. As expected, the STD becomes smaller and smaller going from high-resolution image candidate (d) to low-noise image candidate (a), suggesting more and more noise are suppressed. By contrast, it is not surprised that the resolution becomes higher and higher from the low-noise direction to the high-resolution direction.

It should be emphasized that these different noise-resolution tradeoffs do not mean one image is better than another image for all the tasks. For example, to inspect the curved structure pointed out by the yellow arrow, it might be better to use the two low-noise image candidates (a) and (b), since this structure is distorted by the strong streak artifacts stemmed from the remained structured noise in the default denoised image and the high-resolution image candidate. However, if one want to visualize the structure indicated by the red arrow, the default denoised image (c) and the high-resolution image candidate (d) are preferred, since this structure is blurred in the low-noise direction due to the overly noise suppression process. Moreover, for quantitative comparison, we also calculate the RMSE for all the images by comparing to the NDCT image. It is interesting to find that the default denoised image doesn't have the lowest RMSE value. Instead, the image with the lowest noise, i.e., image candidate (a), has the smallest RMSE values.

Fig. 4 presents the generated image candidates with different noise-resolution tradeoffs for the other image from the validation dataset. We assume here our task is to visualize the high-contrast details as shown with the zoomed-in ROIs. It is clearly demonstrated that the noise is weaker and weaker going from image (d) to image (a). By contrast, the resolution is better and better from (a) to (d). As such, one can choose any image candidate with desired noise-resolution tradeoff to suit for the specific clinical task. For example, as indicated by the red arrow, regarding this point-like structure, the image (c), the high resolution candidate, shows the best discriminativeness, while both the default denoised image (b) and the low-noise image candidate (a) exhibit blurring effects, and the original LDCT (d) is overwhelmed by the strong noise. This gradual transition property can be further quantitatively observed from the STDs associated with a selected flat region indicated by the green solid box in Fig. 4(e). Besides, we also calculated the associated RMSE for each processed image against the NDCT image. It can be found that despite their distinct resolution differences, all the three denoised images have comparable

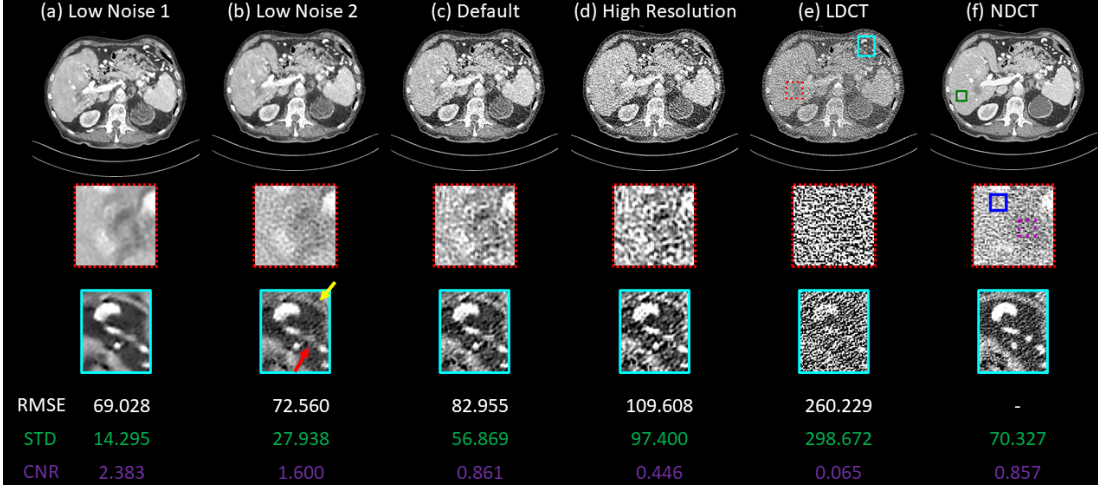


Fig. 3. Generated denoised image candidates with respect to an image in the validation dataset for low-contrast lesion detection task. From left to right, they are (a) low noise 1, (b) low noise 2, (c) default, (d) high resolution image candidates and (e) LDCT, (f) NDCT images. Row 2 shows the zoomed-in views of a low-contrast ROI marked by the red dot box in (e) of Row 1, and Row3 shows the zoomed-in views of a high-contrast ROI marked by the cyan solid box in (e) of Row 1. The STDs are calculated based on a flat region marked by the green solid box in (f) of Row 1. The CNRs are calculated based on the foreground content marked by the purple dot box and the background content marked by the blue solid box in (f) of Row 2. The RMSE values are calculated against the NDCT. Display window: [-160, 240] HU.

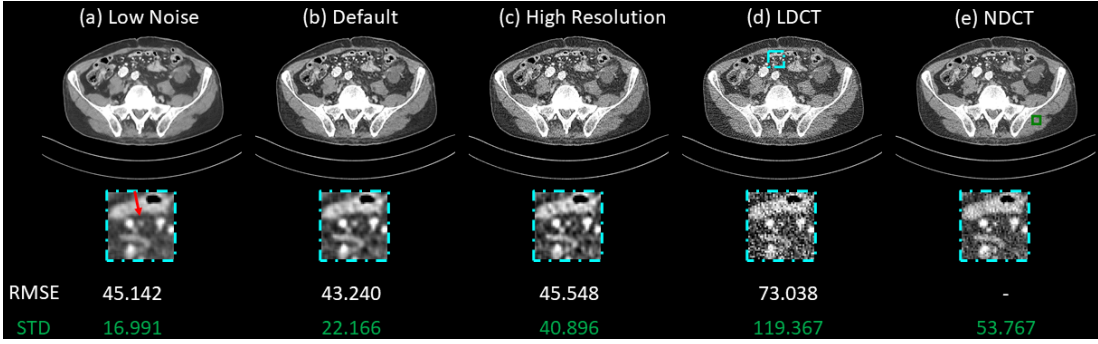


Fig. 4. Generated denoised image candidates with respect to an image in the validation dataset for high-contrast structure inspection. From left to right, (a) low noise, (b) default, (c) high resolution image candidates as well as (d) LDCT and (e) NDCT images. The zoomed-in views below correspond to the ROI marked by the cyan dot dash box in (d) of Row 1. The STDs are calculated based on a flat region specified by the green solid box in (e) of Row 1. The RMSE values are calculated against the NDCT. Display window: [-160, 240] HU.

RMSE values.

Fig. 5 illustrates the denoised results for the images with different NIs from the cadaver study. We can observe that the default model, which was trained to predict the associated NDCT image from the LDCT image of quarter dose level, produces over-smoothed image when the noise of the input image is already very weak, such as the images corresponding to NIs of 10 and 20. While for the images that have relatively stronger noise, such as the images with NIs of 30 and 40, the processed images exhibit overall good noise-resolution tradeoffs. Since our DID algorithm can produce multiple image candidates, we can restore the overly smoothed structures by generating an image candidate towards the high-resolution direction, as indicated by the red arrow as well as the zoomed-in view in the first row of Fig. 5. As for those images which already have overall good noise-resolution tradeoffs, our DID algorithm can still provide other low-noise-preferred or high-resolution-preferred image candidates to adapt to different clinical tasks. For quantitative evaluation, we further calculate the STDs for each image candidate based on a specified flat region, as indicated by the green dash box in each input image. One can observe that, by applying the DID algorithm, the

STDs become smaller and smaller as the image candidates generation direction shifting from the high-resolution direction to the low-noise direction.

Similar phenomena can also be observed from the CBCT dataset-based experiments where multiple images are generated with gradually transiting noise-resolution tradeoffs. See Fig. S1 in the supporting document for details.

Fig. 6 demonstrates our DID algorithm's performance based on a more general network architecture, i.e., plain network. We can clearly observe the gradual transiting phenomenon regarding the noise-resolution tradeoff. To be specific, from the above case that corresponds to the high-contrast slice from the validation dataset, we can see that the high-resolution image candidate reveals clearer structure boundaries, which either are smoothed out in the default image and low-noise image candidate, or are overwhelmed by the strong quantum noise in the original LDCT image. This phenomenon can be further verified from the zoomed-in views of the ROI marked by the cyan dot dash box. It should be mentioned that the high-resolution image candidate might be more clinically useful regarding certain high-resolution-demanded task, despite it has the largest RMSE value among all the illustrated image

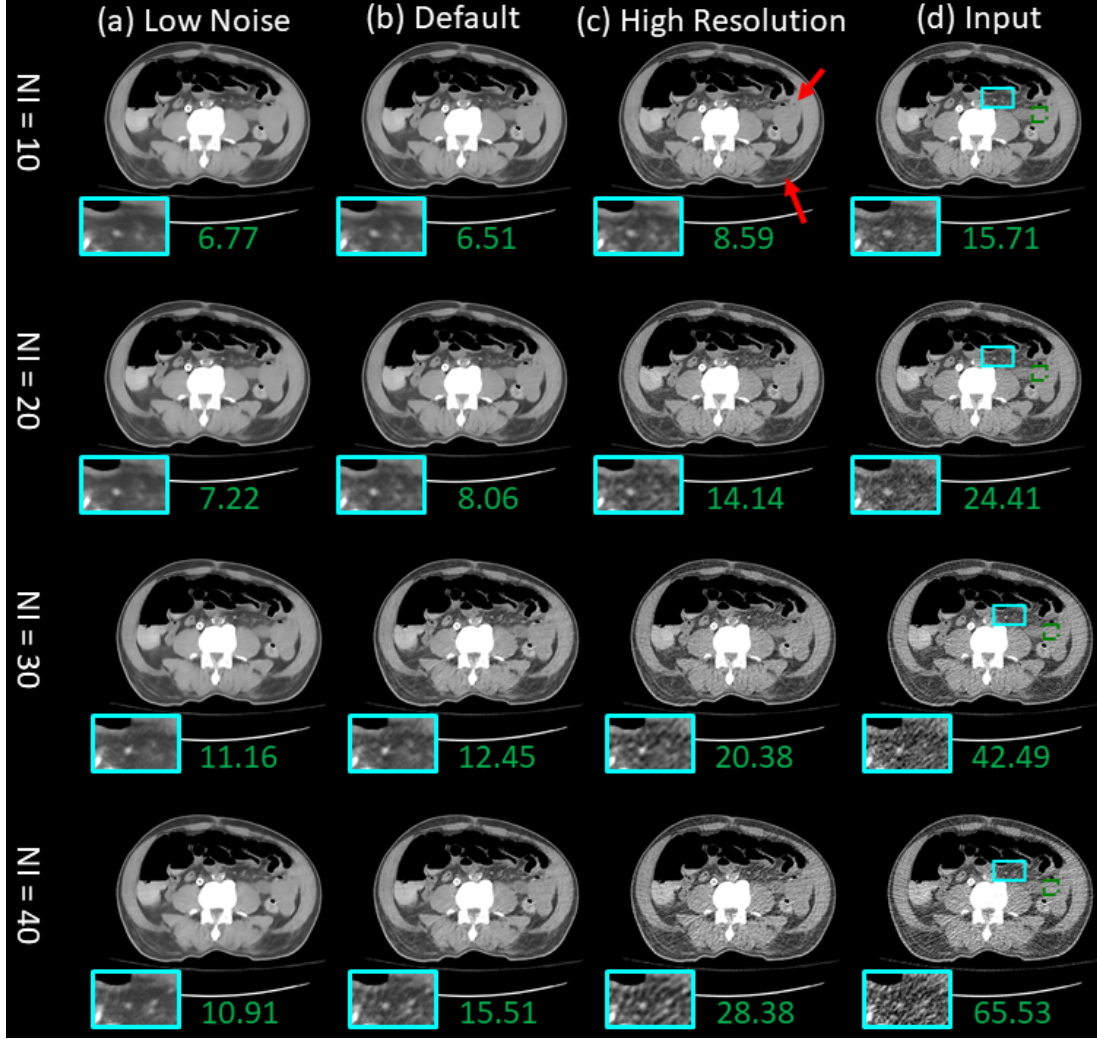


Fig. 5. Generated denoised image candidates for the cadaver study. From left to right, (a) low noise, (b) default, (c) high resolution image candidates and (d) input image. From top to bottom, they correspond to different noise indexes from 10 to 40. The zoomed-in views correspond to the ROI marked by the cyan solid box. The STDs are calculated based on a flat region specified by the green dot dash box. Display window: [-160, 240] HU.

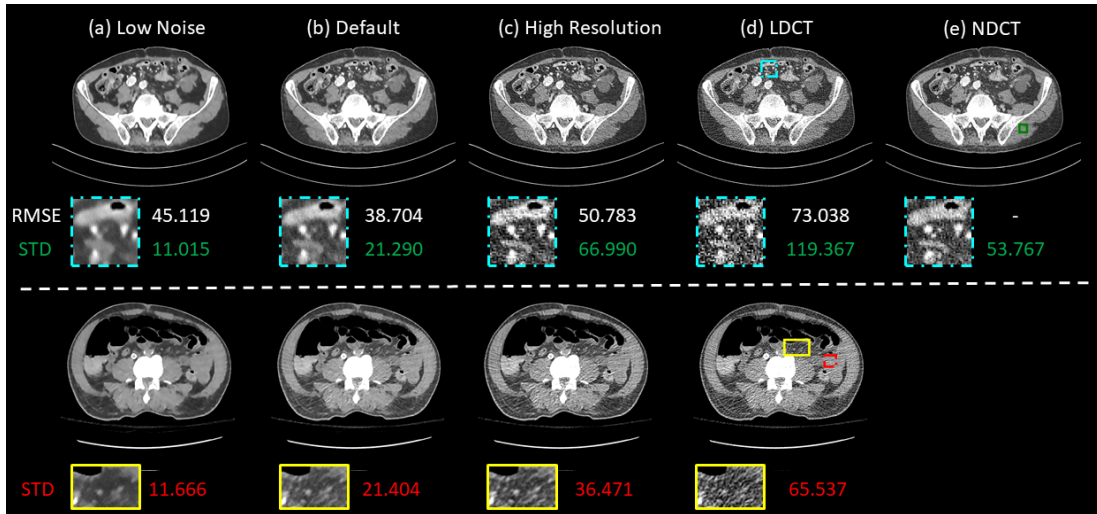


Fig. 6. Generated denoised image candidates with the plain network. From left to right, (a) low noise, (b) default, (c) high resolution image candidates and (d) LDCT, (e) NDCT images. The case above the dash line correspond to an image in the validation dataset for high-contrast structure inspection. The case below the dash line correspond to an image from cadaver study with a noise index of 40. The RMSE values are calculated against the NDCT. The STDs are calculated based on a flat region specified by the green solid box (above) and the red dot dash box (below). The zoomed-in views correspond to the ROI marked by the cyan dot dash box (above) and the ROI marked by the yellow solid box (below). Display window: [-160, 240] HU.

candidates. By visually comparing the high-resolution image candidate with the associated NDCT image, we can find that the former exhibits comparable image resolution while slightly stronger noise. The noise strength comparison can be further quantitatively confirmed based on the STDs of the ROI marked by the green solid box. As for the below case that corresponds to the cadaver study with a NI of 40, it can be observed that all the image candidates have their own values, in terms of: 1) the low-noise image candidate shows well-suppressed image while inferior resolution, 2) the high-resolution image candidate shows superior resolution despite the stronger streaky artifact, and 3) the default denoised image shows intermediate image properties. This observation can be further supported by the zoomed-in view of the ROI marked by the yellow solid box, as well as the STDs of the ROI marked by the red dot dash box.

We now show the adaptation of the proposed DID algorithm on the training datasets with different noise levels. As shown in Fig. 7, as the dose levels of the training datasets decrease from $\frac{1}{2}$ to $\frac{1}{16}$, the default denoised images (b) become smoother and smoother, among which, the image denoised with the model trained on 25% dose level training dataset show overall the best noise-resolution tradeoffs. After we apply the proposed DID algorithm, by selecting a desired image candidate, we can effectively shift this tradeoff to a desired degree for the images processed with models associated with different dose levels. More specifically, for the $\frac{1}{2}$ dose level dataset-based model, one can choose the low-noise image candidate if feels the default denoised image is a little bit noisy. Regarding the models trained based on the $\frac{1}{8}$ or $\frac{1}{16}$ dose level datasets, one can choose the high-resolution image candidates to reveal more details. These phenomena can be more clearly observed from the associated zoomed-in view shown in Fig. 8 for the ROI marked by the cyan dot dash box in Fig. 7.

V. DISCUSSION AND CONCLUSION

It is well accepted that the evaluation of medical image quality is highly task specific, and sometimes even user specific depending on their clinical experience and image appearance preference. Benefited from the rapid development of DL techniques, AI-based automation tools have been largely developed for healthcare. However, there still exists obstacles for their clinical deployment. One of the reasons might be that AI usually can only provide a general result which reflects the overall properties of the training dataset. Since the final useable result is usually task-specific and user-specific, a further customization based on this general result is essential. We believe human-centered AI in medicine is the way to go for the clinical implementation of AI technologies, where AI will not replace human by fully automating everything, instead, it will assist human to perform clinical tasks better and faster.

Regarding the medical image denoising task, many excellent DL-based denoisers have been developed. Compared to the conventional methods, these DL-based automatic denoisers show generally superior performance when the training and testing environments are consistent (such as the default denoised images defined in this paper). However, they cannot deliver task-specific and user-specific results since they usually can only produce one single output which reflects the overall

properties of the training dataset. Besides, their performance will be decreased when there exists dataset domain shift. Realized these challenges, in this study, on top of existing DL-based denoisers, we proposed the DID algorithm that can assist users to interactively tune the images to achieve the noise-resolution tradeoff desired for the specific task.

This is achieved by solving problems (4) and (5) during the testing phase as detailed in the Sec. II-A. Since our DID algorithm is directly used in the model testing phase, does not need to interrupt the training pipelines of any existing models, thereby it can be readily combined with any state-of-the-art DL-based denoisers. This property has been demonstrated in this work by checking the algorithm's performance based on two different but popular network architectures (U-Net as shown in Figs. 3 to 5 and plain network as shown in Fig. 6).

Moreover, the proposed DID algorithm can also be used to mitigate the model generalizability issue which has been widely recognized in the DL-based denoisers. Basically, by learning from the training dataset, the DL-based denoisers are trained to suppress the noise of a CT image, and are only expected to reach the overall optimal (in terms of some predefined metrics, such as RMSE in this paper) denoising performance when the noise levels of the LDCT images in the training dataset and of the testing images are the same. However, in practice, different LDCT scans may have different noise levels due to different anatomical sites, equipment vendors, and imaging protocols and so on. It is also likely that different slices from the same CT scan may also have different noise levels due to tube current modulation. A model trained to target a specific noise level would have the generalizability issue to handle these miscellaneous scenarios. As demonstrated in Fig. 5, our U-Net model, which was trained based on a simulated training dataset, would overly smoothen the anatomical structures when the NIs of the input CT images were 10 or 20, while can produce an denoised image with relatively balanced tradeoff when the associated NIs were 30 or 40. Similar phenomena can also be observed from the CBCT study shown in Fig. S1 in the supporting documents, i.e., the model would smooth out the structures when the exposure levels were $\frac{1}{2}$ or $\frac{1}{4}$, and produce balanced results when the exposure level was $\frac{1}{8}$. Generally speaking, if the model is trained to deal with stronger noise, it will tend to overly denoise the image, and thereby render a smoothed-out result when the noise of the input image is weaker than those of the training images, and vice versa. For instance, as shown in Fig. 7, the model trained based on $\frac{1}{16}$ ($\frac{1}{2}$) dose level dataset would result in overly smoothed (slightly noisy) image when the input LDCT has a quarter dose level. Since our DID algorithm can generate multiple image candidates with different noise-resolution tradeoffs, it is expected to mitigate this generalizability issue by choosing an appropriate image candidate with desired property instead of the default over/under-denoised image. For example, as shown in Fig. 5, one can choose the high-resolution image candidates for the input images with NIs of 10 and 20, and the low-noise image candidates for the input image with NI of 40.

To enable a smooth and friendly interactive user experience between the model and the physician, computational efficiency

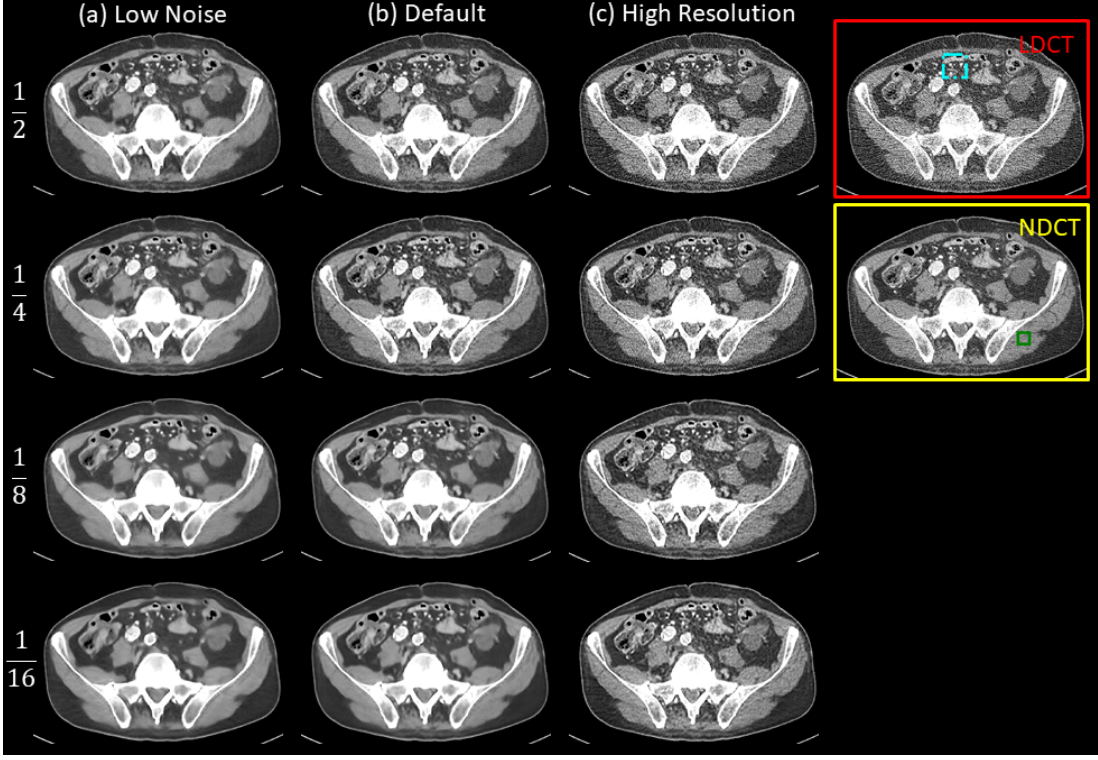


Fig. 7. Generated denoised image candidates with different training datasets that have different noise levels. From left to right, (a) low noise, (b) default, (c) high resolution image candidates. The LDCT and NDCT images are illustrated on the right-most column. From top to bottom, each row corresponds to a different training dataset with a different dose level setting, from $\frac{1}{2}$ to $\frac{1}{16}$ of the NDCT. The testing image has a dose level of $\frac{1}{4}$ compared to the NDCT. Display window: [-160, 240] HU.

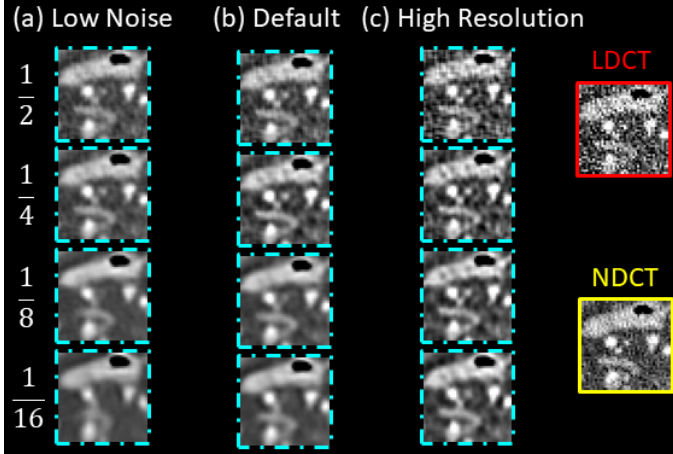


Fig. 8. Zoomed-in view for the ROIs marked by the cyan dot dash box in Fig. 7. From left to right, (a) low noise, (b) default, (c) high resolution image candidates. The LDCT and NDCT images are illustrated on the right-most column. From top to bottom, rows correspond to different training datasets with dose level settings, changing from $\frac{1}{2}$ to $\frac{1}{16}$ of the NDCT. The testing image has a dose level of $\frac{1}{4}$ compared to the NDCT. Display window: [-160, 240] HU.

plays a vital role. In this work, we use the U-Net as the default architecture with an input size of 512×512 . It only takes tens of milliseconds per iteration while solving problems (4) and (5) by using a single NVIDIA Titan X GPU card. This can be considered as a real-time image generation. One can use some other heavier or lighter model architectures for potential better model performance or efficiency. Besides, one can also pre-generate all the image candidates and store them into the local drive, such that the physician can browse them back-

and-forth without any time delay.

Except the computation efficiency, another way to improve the user experience is to quantify the noise-resolution tradeoff of the resultant image with some simple and understandable metrics. This can greatly help the physician quickly locate the desired image candidate. This is beyond the scope of this paper, and we will keep it as a further potential research direction.

Lastly, in this work, we use the DL-based denoiser to prove the concept of deep interactive denoising. Indeed, theoretically speaking, one can easily extend the proposed DID algorithm to refine the default results for other conventional denoisers.

In summary, in this paper, our target is to develop a human-centered AI-based denoiser that can interact with the physicians for task-specific denoising. To achieve this goal, we introduced an optimization process into the testing phase, such that multiple images can be generated with various noise-resolution trade-offs from a default denoised image produced by a pre-trained denoiser. Experimental results involved multiple simulation and realistic patient datasets demonstrated that the proposed algorithm can deliver multiple image candidates with different noise-resolution tradeoffs, which can be used for task-specific applications. Additionally, the results also showed the superior generalizability of our algorithm since it can adapt to different architectures, different training and testing datasets with different noise levels.

ACKNOWLEDGMENT

We would like to thank Dr. Chenyang Shen for instructive discussions and Dr. Jonathan Feinberg for editing the

manuscript.

REFERENCES

- [1] C. You, Q. Yang, H. Shan, L. Gjestebj, G. Li, S. Ju, Z. Zhang, Z. Zhao, Y. Zhang, W. Cong, and G. Wang, "Structurally-sensitive multi-scale deep neural network for low-dose ct denoising," *IEEE Access*, vol. 6, pp. 41 839–41 855, 2018.
- [2] I. A. Elbakri and J. A. Fessler, "Statistical image reconstruction for polyenergetic x-ray computed tomography," *IEEE transactions on medical imaging*, vol. 21, no. 2, pp. 89–99, 2002.
- [3] J. Wang, H. Lu, T. Li, and Z. Liang, "Sinogram noise reduction for low-dose ct by statistics-based nonlinear filters," in *Medical Imaging 2005: Image Processing*, vol. 5747. International Society for Optics and Photonics, Conference Proceedings, pp. 2058–2066.
- [4] H. R. Dufan Wu and Q. Li, "Self-supervised dynamic ct perfusion image denoising with deep neural networks," *ArXiv*, vol. 2005.09766v1, 2020.
- [5] A. Manduca, L. Yu, J. D. Trzasko, N. Khaylova, J. M. Koffler, C. M. McCollough, and J. G. Fletcher, "Projection space denoising with bilateral filtering and ct noise modeling for dose reduction in ct," *Medical physics*, vol. 36, no. 11, pp. 4911–4919, 2009.
- [6] G. Chen, J. Tang, and S. Leng, "Prior image constrained compressed sensing (piccs): a method to accurately reconstruct dynamic ct images from highly undersampled projection data sets," *Medical physics*, vol. 35, no. 2, pp. 660–663, 2008.
- [7] J. Wang, T. Li, H. Lu, and Z. Liang, "Penalized weighted least-squares approach to sinogram noise reduction and image reconstruction for low-dose x-ray computed tomography," *IEEE transactions on medical imaging*, vol. 25, no. 10, pp. 1272–1283, 2006.
- [8] M. Kumar and M. Diwakar, "A new locally adaptive patch variation based ct image denoising," *International Journal of Image, Graphics and Signal Processing*, vol. 8, no. 1, p. 43, 2016.
- [9] Q. Xu, H. Yu, X. Mou, L. Zhang, J. Hsieh, and G. Wang, "Low-dose x-ray ct reconstruction via dictionary learning," *IEEE transactions on medical imaging*, vol. 31, no. 9, pp. 1682–1697, 2012. [Online]. Available: <https://www.ncbi.nlm.nih.gov/pmc/articles/PMC3777547/pdf/nihms509576.pdf>
- [10] H. Chen, Y. Zhang, M. K. Kalra, F. Lin, Y. Chen, P. Liao, J. Zhou, and G. Wang, "Low-dose ct with a residual encoder-decoder convolutional neural network," *IEEE Transactions on Medical Imaging*, vol. 36, no. 12, pp. 2524–2535, 2017.
- [11] H. Chen, Y. Zhang, W. Zhang, P. Liao, K. Li, J. Zhou, and G. Wang, "Low-dose ct via convolutional neural network," *Biomedical Optics Express*, vol. 8, no. 2, pp. 679–694, 2017. [Online]. Available: <http://www.osapublishing.org/boe/abstract.cfm?URI=boe-8-2-679>
- [12] S. L. Wang and Guobao, "Low-dose ct image denoising using parallel-clone networks," *ArXiv*, vol. 2005.06724v1, 2020.
- [13] Q. Yang, P. Yan, Y. Zhang, H. Yu, Y. Shi, X. Mou, M. K. Kalra, Y. Zhang, L. Sun, and G. Wang, "Low-dose ct image denoising using a generative adversarial network with wasserstein distance and perceptual loss," *IEEE Transactions on Medical Imaging*, vol. 37, no. 6, pp. 1348–1357, 2018.
- [14] Y. Li, K. Li, C. Zhang, J. Montoya, and G.-H. Chen, "Learning to reconstruct computed tomography (ct) images directly from sinogram data under a variety of data acquisition conditions," *IEEE transactions on medical imaging*, 2019.
- [15] J. Wang, T. Li, and L. Xing, "Iterative image reconstruction for cbct using edge-preserving prior," *Medical physics*, vol. 36, no. 1, pp. 252–260, 2009.
- [16] E. Y. Sidky and X. Pan, "Image reconstruction in circular cone-beam computed tomography by constrained, total-variation minimization," *Physics in Medicine and Biology*, vol. 53, no. 17, p. 4777, 2008.
- [17] X. Jia, B. Dong, Y. Lou, and S. B. Jiang, "Gpu-based iterative cone-beam ct reconstruction using tight frame regularization," *Physics in Medicine and Biology*, vol. 56, no. 13, p. 3787, 2011.
- [18] M. Diwakar and M. Kumar, "Edge preservation based ct image denoising using wiener filtering and thresholding in wavelet domain," in *2016 Fourth International Conference on Parallel, Distributed and Grid Computing (PDGC)*. IEEE, Conference Proceedings, pp. 332–336.
- [19] E. Y. Sidky, Y. Duchin, X. Pan, and C. Ullberg, "A constrained, total-variation minimization algorithm for low-intensity x-ray ct," *Medical physics*, vol. 38, no. S1, pp. S117–S125, 2011.
- [20] H. Shan, A. Padole, F. Homayounieh, U. Kruger, R. D. Khera, C. Nitwarangkul, M. K. Kalra, and G. Wang, "Competitive performance of a modularized deep neural network compared to commercial algorithms for low-dose ct image reconstruction," *Nature Machine Intelligence*, vol. 1, no. 6, pp. 269–269, 2019.
- [21] T. Niu and L. Zhu, "Accelerated barrier optimization compressed sensing (abocs) reconstruction for cone-beam ct: Phantom studies," *Medical physics*, vol. 39, no. 7Part2, pp. 4588–4598, 2012.
- [22] H. Shan, Y. Zhang, Q. Yang, U. Kruger, M. K. Kalra, L. Sun, W. Cong, and G. Wang, "3-d convolutional encoder-decoder network for low-dose ct via transfer learning from a 2-d trained network," *IEEE Transactions on Medical Imaging*, vol. 37, no. 6, pp. 1522–1534, 2018.
- [23] J. Kim, J. K. Lee, and K. M. Lee, "Accurate image super-resolution using very deep convolutional networks," pp. 1646–1654, 2015.
- [24] A. Vaswani, N. Shazeer, N. Parmar, J. Uszkoreit, L. Jones, A. N. Gomez, L. Kaiser, and I. Polosukhin, "Attention is all you need," in *Advances in neural information processing systems*, Conference Proceedings, pp. 5998–6008.
- [25] S. Ioffe and C. Szegedy, "Batch normalization: Accelerating deep network training by reducing internal covariate shift," *Computer Science*, 2015.
- [26] D. Ulyanov, A. Vedaldi, and V. Lempitsky, "Deep image prior," *International Journal of Computer Vision*, 2020.
- [27] Y. Lecun, Y. Bengio, and G. Hinton, "Deep learning," *Nature*, vol. 521, no. 7553, pp. 436–44, 2015.
- [28] K. He, X. Zhang, S. Ren, and J. Sun, "Deep residual learning for image recognition," *Computer Science*, 2015.
- [29] L. C. Chen, G. Papandreou, I. Kokkinos, K. Murphy, and A. L. Yuille, "Deeplab: Semantic image segmentation with deep convolutional nets, atrous convolution, and fully connected crfs," *IEEE Trans Pattern Anal Mach Intell*, vol. 40, no. 4, pp. 834–848, 2016.
- [30] S. Ren, K. He, R. Girshick, and J. Sun, "Faster r-cnn: Towards real-time object detection with region proposal networks," *IEEE Transactions on Pattern Analysis and Machine Intelligence*, pp. 1–1, 2016.
- [31] J. Long, E. Shelhamer, and T. Darrell, "Fully convolutional networks for semantic segmentation," in *Proceedings of the IEEE conference on computer vision and pattern recognition*, Conference Proceedings, pp. 3431–3440.
- [32] A. Krizhevsky, I. Sutskever, and G. E. Hinton, "Imagenet classification with deep convolutional neural networks," *Advances in Neural Information Processing Systems*, vol. 25, no. 2, pp. 2012–2022, 2012.
- [33] K. Simonyan and A. Zisserman, "Very deep convolutional networks for large-scale image recognition," *Computer Science*, 2014.
- [34] C. You, G. Li, Y. Zhang, X. Zhang, H. Shan, M. Li, S. Ju, Z. Zhao, Z. Zhang, W. Cong, M. W. Vannier, P. K. Saha, E. A. Hoffman, and G. Wang, "Ct super-resolution gan constrained by the identical, residual, and cycle learning ensemble (gan-circle)," *IEEE Transactions on Medical Imaging*, vol. 39, no. 1, pp. 188–203, 2020.
- [35] H. Chen, Y. Zhang, Y. Chen, J. Zhang, W. Zhang, H. Sun, Y. Lv, P. Liao, J. Zhou, and G. Wang, "Learn: Learned experts' assessment-based reconstruction network for sparse-data ct," *IEEE Transactions on Medical Imaging*, vol. 37, no. 6, pp. 1333–1347, 2018.
- [36] E. Y. Sidky, C.-M. Kao, and X. Pan, "Accurate image reconstruction from few-views and limited-angle data in divergent-beam ct," *Journal of X-ray Science and Technology*, vol. 14, no. 2, pp. 119–139, 2006.
- [37] T. Bai, H. Yan, X. Jia, S. Jiang, G. Wang, and X. Mou, "Z-index parameterization for volumetric ct image reconstruction via 3-d dictionary learning," *IEEE Transactions on Medical Imaging*, vol. 36, no. 12, pp. 2466–2478, 2017.
- [38] A. Jacot, F. Gabriel, and C. Hongler, "Neural tangent kernel: Convergence and generalization in neural networks," in *Advances in neural information processing systems*, 2018, pp. 8571–8580.
- [39] M. D. Julián Tachella, Junqi Tang, "The neural tangent link between cnn denoisers and non-local filters," *ArXiv*, vol. 2006.02379v4, 2020.
- [40] P. Milanfar, "A tour of modern image filtering: New insights and methods, both practical and theoretical," *IEEE Signal Processing Magazine*, vol. 30, no. 1, pp. 106–128, 2013.
- [41] B. Chen, X. Duan, Z. Yu, S. Leng, L. Yu, and C. McCollough, "Technical note: Development and validation of an open data format for ct projection data," *Med Phys*, vol. 42, no. 12, pp. 6964–72, 2015. [Online]. Available: <https://www.ncbi.nlm.nih.gov/pubmed/26632052>
- [42] O. Ronneberger, P. Fischer, and T. Brox, "U-net: Convolutional networks for biomedical image segmentation," in *International Conference on Medical Image Computing and Computer-Assisted Intervention*, Conference Proceedings, pp. 234–241.
- [43] D. Ulyanov, A. Vedaldi, and V. Lempitsky, "Instance normalization: The missing ingredient for fast stylization," *arXiv preprint arXiv:1607.08022*, 2016.
- [44] D. Kingma and J. Ba, "Adam: A method for stochastic optimization," *Computer Science*, 2014.